

On the Formation of Coherent Vortices beneath Nonbreaking Free-Propagating Surface Waves

WU-TING TSAI, GUAN-HUNG LU, JHENG-RONG CHEN, AND ALBERT DAI

Department of Engineering Science and Ocean Engineering, National Taiwan University, Taipei, Taiwan

WILLIAM R. C. PHILLIPS

Department of Mathematics, Swinburne University of Technology, Hawthorn, Victoria, Australia

(Manuscript received 1 November 2016, in final form 9 January 2017)

ABSTRACT

Numerical simulations of monochromatic surface waves freely propagating over an initially quiescent flow field are conducted and found to reveal an array of quasi-streamwise vortices of alternating orientation in a manner akin to that of Langmuir circulation beneath wind-driven surface waves. A linear instability analysis of the wave-averaged Craik–Leibovich (CL) equation is then conducted to determine whether the structures in the simulations can be explained by the Craik–Leibovich type 2 (CL2) instability, which requires the presence of spanwise-independent drift and mean shear of the same sign. There is no imposed shear in the simulations, but they confirm the theoretical analysis of Longuet-Higgins that an Eulerian-mean shear with a magnitude comparable to that of Lagrangian Stokes drift occurs at the edge of the surface boundary layer in the otherwise irrotational oscillatory flow. The spanwise wavelength of the least stable disturbance is found to be close to the spacing between predominant vortex pairs, which likely are excited by the CL2 instability.

1. Introduction

Tsai et al. (2015) recently conducted a numerical simulation of monochromatic, finite-amplitude surface waves propagating over an initially quiescent flow field. Their intent was to determine the impact of nonbreaking waves on vorticity generation and, consequently, turbulence production. Their simulation predicted growth rates of turbulent kinetic energy consistent with those measured by Savelyev et al. (2012) using thermal-marking velocimetry. Accordingly both studies depict spanwise intensity levels near the surface well in excess of streamwise levels. Such an occurrence is the hallmark of an array of streamwise vortices of alternating orientation beneath the water surface. The free-surface footprints of those vortices appear as elongated surface streaks both in the simulations and the experiment. Of interest in the present work is the mechanism by which these vortices form.

The footprints and vortices are evident in Fig. 1, which depicts numerical simulations of two cases, namely,

wind-driven (Tsai et al. 2013) and free-propagating surface waves (Tsai et al. 2015). More specifically, Fig. 1 shows views of the elevation of the free surface, along with distributions of temperature fluctuations (upper two panels) and streamwise-averaged distributions of the vertical velocity (lower two panels). The key difference between the two cases is that tangential and normal stresses are present on the surface of wind-driven waves and absent there on free-propagating waves. Nevertheless, up- and downwelling resulting from streamwise-oriented rolls and the characteristic streaky surface signatures due to them are evident in both cases. Of course, there are differences: the rolls are weaker beneath free-propagating waves. Indeed, the level of their average vorticity is an order of magnitude weaker. Moreover, the vortices beneath wind-driven waves penetrate deeper into the layer. Finally, the temperature and velocity fields beneath wind-driven waves reveal wispy finescale filaments, apparently associated with turbulence production by wind shear. We view these vortices as akin to Langmuir circulation (Langmuir 1938), which are wind-aligned, counter-rotating rolls beneath wind-driven surface waves.

Corresponding author address: Wu-ting Tsai, wtsai@ntu.edu.tw

DOI: 10.1175/JPO-D-16-0242.1

© 2017 American Meteorological Society. For information regarding reuse of this content and general copyright information, consult the [AMS Copyright Policy](http://www.ametsoc.org/PUBSReuseLicenses) (www.ametsoc.org/PUBSReuseLicenses).

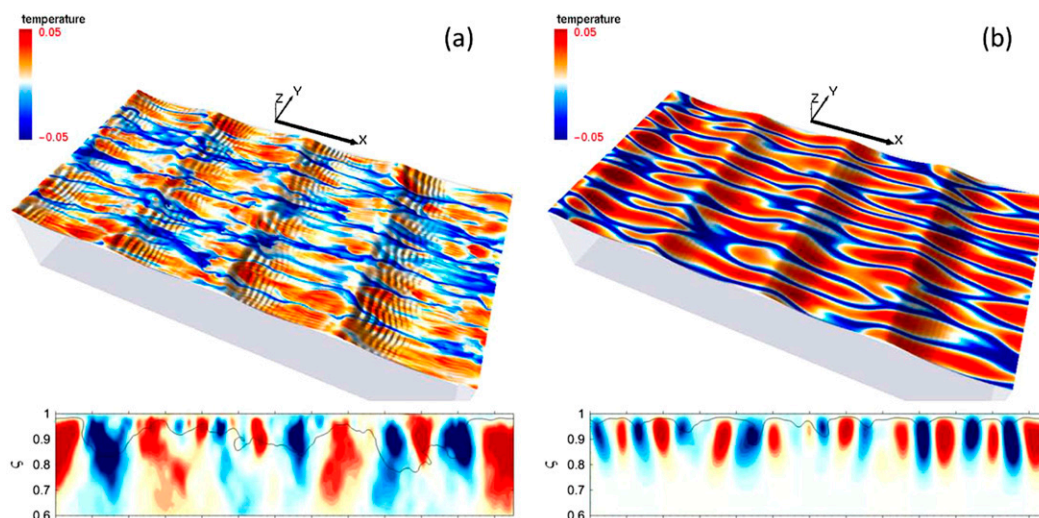


FIG. 1. Comparison between (a) wind-driven (Tsai et al. 2013) and (b) free-propagating surface waves (Tsai et al. 2015). (top) Numerical simulations showing the prospective views of surface elevations and temperature distributions and (bottom) streamwise-averaged distributions of vertical velocity. Regions of red and blue colors represent upwelling and downwelling, respectively. The waves propagate in the positive x direction.

It is widely accepted that Langmuir circulation arises through the interaction of Lagrangian drift of the surface waves with mean shear in the near-surface layer imparted by the wind. The equations that govern Langmuir circulation beneath irrotational surface waves in the presence of weak shear were first derived by Craik and Leibovich (1976) and generalized by Phillips (1998, 2001b) to allow for rotational waves of any amplitude in the presence of shear of any level. The former are known as the Craik–Leibovich (CL) equations and the generalized set is known as the CLg equations. Both sets are mean field or wave-averaged equations, in the sense that they exploit the fact that the primary mean flow and Langmuir circulation evolve over long time scales, with respect to the wave period, and so take a Lagrangian average over the wave. The rectified effect of the wave field is then exposed as the drift.

The CL equations admit two instability mechanisms, Craik–Leibovich type 1 and 2 (CL1 and CL2), according to whether the drift varies laterally or not. Since the latter is closely realized in a random spectrum of waves, CL2 is considered the more likely to occur in nature and is thus the most studied and is the one considered here. On the other hand, when the shear is strong, as in the case of wind-driven Langmuir circulation in the laboratory (Melville et al. 1998), the Langmuir circulation further acts to modulate the imposed wave field in a manner described by the more complicated CLg instability (Craik 1982; Phillips and Wu 1994; Phillips and Shen 1996; Phillips 1998, 2005), a feature first observed by experimentally by Veron and Melville (2001).

For instability, CL2 requires that the differential drift and shear be of the same sign (Leibovich 1983) over at

least a portion of the mixed region (Phillips and Dai 2014). Our simulations, on the other hand, have no imposed shear. Nevertheless, Langmuir circulation are observed not only by us but have also been observed in the open ocean in the absence of wind (Plueddemann et al. 1996). Langmuir turbulence (a discrete spectra of Langmuir circulation) is also evident in the rapid distortion theory study by Teixeira and Belcher (2002) of the interaction of turbulence with a monochromatic irrotational surface wave. But, in fact, the free-surface boundary condition ensures that there always is a shear flow (Longuet-Higgins 1953). As Craik (1982) describes it, the viscous diffusion of momentum owing to the free-surface boundary condition generates a wave-amplitude squared surface stress that in turn produces a second-order Eulerian shear current. This Eulerian-mean flow is discussed further in the context of Langmuir circulation by Phillips (2002). Thus, although not explicitly imposed, our simulations have both an embedded shear and drift and are susceptible to CL2.

In this study, we investigate whether linear stability analysis of the CL equation is able to explain the vortices found in numerical simulations of the full flow system studied by Tsai et al. (2015) and found experimentally in the study by Savelyev et al. (2012). We find that streak spacing (two cells) determined numerically and experimentally are consistent with those arising through the CL2 instability.

2. Numerical simulations

We consider a progressive monochromatic surface wave on an incompressible viscous fluid, and the

three-dimensional flow field that evolves from an initially quiescent state beneath it. The flow field is determined by solving the primitive Navier–Stokes momentum equations subject to solenoidal constraint and the fully nonlinear boundary conditions on the exact wavy surface $z = \eta(x, y, t)$. Here, x and y lie on the mean free surface with x in the direction of wave propagation, z is vertical positive up, and t is time. Further, because buoyancy due to temperature fluctuations does not modify the vertical momentum equation, temperature is treated as a passive tracer. The numerical model employs spectral discretization for horizontal differentials and finite differencing in the vertical with a mesh fine enough to resolve gravity–capillary waves down to capillary scale and the viscous sublayer immediately beneath the wavy surface (Tsai and Hung 2007). The numerical implementations for the simulation are the same as those in Tsai et al. (2015).

Tsai et al. (2015) considered a periodic surface wave of wavelength $\lambda = 7.5$ cm with an initial steepness $\varepsilon = ak = 0.25$, where a is the wave amplitude and the wavenumber $k = 2\pi\lambda^{-1}$. In this study, the initial steepness is unchanged, and four wavelengths are considered, namely, $\lambda = 7.5, 12.5, 15,$ and 20 cm, with respective amplitude-based wave Reynolds numbers $\text{Re}_w = a^2\omega_0\nu^{-1} = 255, 550, 722,$ and 1111 . Here, $\omega_0 = (gk)^{1/2}$ is the angular frequency, g is gravity, and ν is the kinematic viscosity of water. The size of the computational domain is $4\lambda, 2\lambda,$ and 0.8λ in, respectively, the streamwise x , spanwise y , and vertical z directions. The total number of discretized grid points is $(512 \times 256 \times 128)$ for the case of $\lambda = 7.5$ cm, which increases to $(576 \times 288 \times 128)$ for the cases of $\lambda = 12.5$ and 15 cm and to $(768 \times 383 \times 192)$ for the longest wave, $\lambda = 20$ cm, considered.

The numerical simulations are initialized using the velocity field and surface deformation of a Stokes wave. Superimposed on that flow field are ambient disturbances whose amplitudes are homogeneous in the horizontal directions and decay downward. To set up the initial ambient disturbances, the evolution of a solenoidal random velocity field beneath a free-slip surface is first computed, as described in Tsai et al. (2005), and rescaled such that its kinetic energy is about 0.1% of the total energy. The superimposed random disturbances decay rapidly during the spinup computation. The monochromatic surface waves therefore develop over a disturbed quiescent flow field with a fluctuation energy about 0.01% of the total energy. No prescribed flow structures with predominant unstable length scales exist in the flow field. Computations were continued until the flow was statistically stationary.

3. Coherent vortical structures

Of particular interest are streamwise-oriented, counterrotating vortices, which form in the near-surface region and live over time scales that are long with respect to the wave period. Such vortices, or coherent structures, are composed of rolls determined by v and w and streaks given by u ; the velocity components (u, v, w) are in the (x, y, z) directions. Since the vortices give rise to distinctive footprints at the free surface, we begin by viewing in Fig. 1 the free surface and the footprints on it, as reflected by the distribution of temperature (upper panels). To further show that the footprints are a reflection of robust long-living structures beneath the waves, we include streamwise averages of w (lower panels). The results in Fig. 1 are for $\lambda = 7.5$ cm, but the surface and flow structures and the computed statistics of the additionally simulated waves ($\lambda = 12.5, 15,$ and 20 cm) are much the same and concur with those reported in Tsai et al. (2015). Finally, for comparison, we include a wind-driven case.

Looking first at the free surface, we see that although elongated regions in x are evident in both cases, the pattern is more distinctive in the case of free-propagating surface waves (Fig. 1b). This means that energy is largely confined to one spanwise wavenumber (with the remainder in larger disparate wavenumbers) rather than distributed over a discrete spectrum of wavenumbers of similar value, as would appear to be the case with wind forcing (Fig. 1a). Further insight into whether energy is redistributed largely into one or a spectrum of wavenumbers is seen in the surface elevation of the waves, which began monochromatic but do not remain so. Specifically, while the amplitudes of newly excited harmonics are barely visible in Fig. 1b, they are not only clearly evident in Fig. 1a but vary in y . This spanwise variation is reminiscent of the CLg instability, in which the streamwise structures, which are here deeper and more extensive than those in Fig. 1b, modulate the wave field. On the other hand, the absence of modulation in free-propagating waves is consistent with the CL2 instability.

Tsai et al. (2015) identified these streamwise structures as pairs of counterrotating, streamwise vortices (see their Fig. 5) and noted that the distinctive elongated streaks on the surface result from them. In Fig. 2, we see that the same characteristic surface footprints are evident in the infrared images of Savelyev et al. (2012).

To further reveal the ubiquity of these vortices, iso-surfaces of the streamwise vorticity field ω_x at the time instance $t = 20T_0$ are shown in Fig. 3 for progressive waves with $\lambda = 7.5$ and 20 cm. Here, $T_0 = 2\pi\omega_0^{-1}$ is the linear wave period of the progressive wave. Two representative vorticities of opposite sign but the same

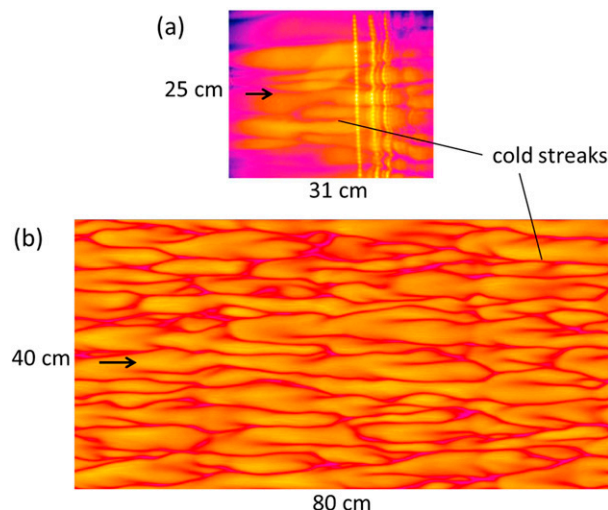


FIG. 2. (a) Infrared image of the water surface taken by Savelyev et al. (2012) and (b) surface temperature distribution from the present numerical simulation showing the elongated thermal streaks. The infrared image of Savelyev et al. (2012) has been turned such that the waves propagate from left to right in both images. The color map of the simulated temperature distribution is adjusted to resemble that of the infrared image.

absolute value are depicted, namely, vorticity strengths of one-eighth of the second-order, Eulerian-mean shear immediately beneath the boundary layer at the water surface, that is, from (5): $\omega_x = \pm 0.25\omega_0 a^2 k^2$. The origin of this shear will be discussed in next section.

The isosurfaces appear in the form of elongated tubes, which extend in the wave-propagating direction and modulate in a manner that follows the elevation of the wavy surface. The modulation further suggests vortex strength has a maximum near the trough and minimum near the crest. The temporal array of streamwise, counterrotating vortices densely covers all parts immediately beneath the surface. However, more elongated vortex pairs per wavelength of surface wave are observed beneath the longer surface wave $\lambda = 20$ cm, which suggests that the transverse spacing between vortex pairs d_s is a characteristic length scale of the coherent flow structure.

To quantify this characteristic length scale, the disturbance velocity $\mathbf{v}'(x, y, \zeta, t)$ in the domain of the wave-following vertical coordinate $\zeta = (z + H)(\eta + H)^{-1}$, where H denotes the water depth, is defined by subtracting both the mean component $\bar{\mathbf{v}}(\zeta, t)$ and the wave-correlated component $\hat{\mathbf{v}}(x, \zeta, t)$ from the total velocity $\mathbf{v}(x, y, \zeta, t)$, namely, $\mathbf{v}' = \mathbf{v} - \bar{\mathbf{v}} - \hat{\mathbf{v}}$. Here, the mean component $\bar{\mathbf{v}}(\zeta, t)$ is the average over the x - y plane, and the wave-correlated component is the difference between the phase average over spanwise y and the mean component: $\hat{\mathbf{v}}(x, \zeta, t) = \langle \mathbf{v} \rangle_y(x, \zeta, t) - \bar{\mathbf{v}}(\zeta, t)$.

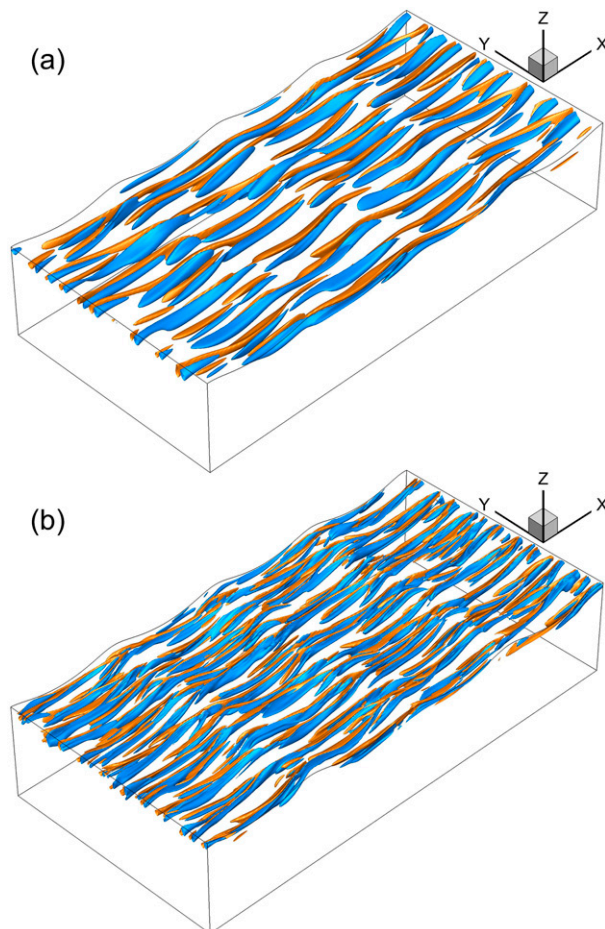


FIG. 3. Isosurface distributions of streamwise vorticity at the time instance $t = 20T_0$ for the cases of wavelength $\lambda =$ (a) 7.5 and (b) 20 cm. The vorticity strength is one-eighth of the second-order, Eulerian-mean shear immediately beneath the boundary layer at the water surface [(5)], that is, $\omega_x = \pm 0.25\omega_0 a^2 k^2$. The waves propagate in the positive x direction. The width (length in y direction) is 2λ in both panels. The orange/blue color represents positive/negative vorticity. The orientation of positive vorticity is counterclockwise facing upstream (negative x direction).

The transverse wavenumber of the predominant coherent flow structure can then be quantified by

$$l_s(t) = \frac{\int l S(l, t) dl}{\int S(l, t) dl}, \quad (1)$$

where integration is taken over all l , and the streamwise-averaged power spectral density of the disturbance velocity field is

$$S(l, t) = \left\langle \int \hat{\mathbf{v}}'(x, l, \zeta, t) \hat{\mathbf{v}}'^*(x, l, \zeta, t) d\zeta \right\rangle_x, \quad (2)$$

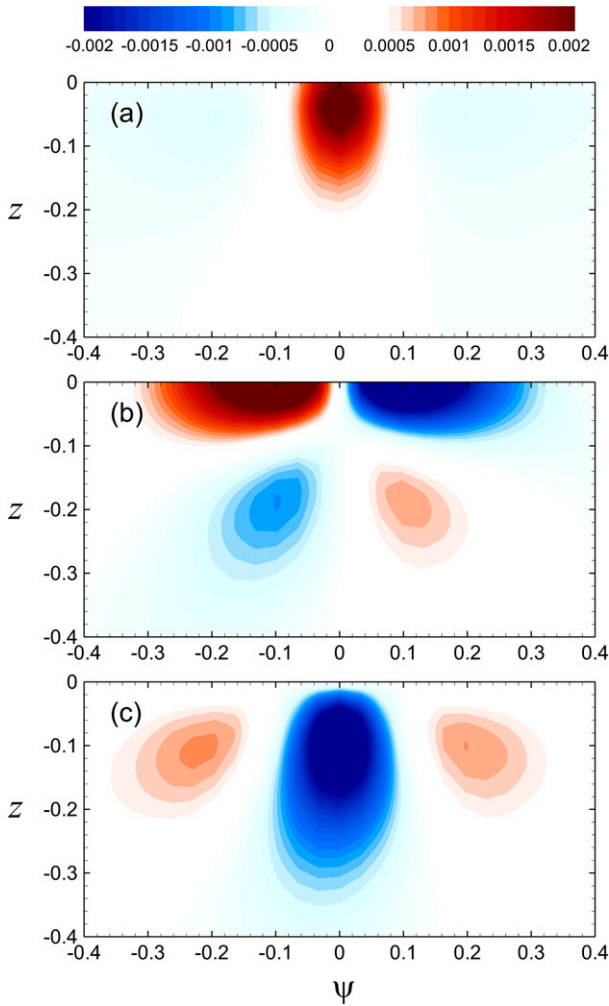


FIG. 4. Conditionally averaged distributions of fluctuating (a) streamwise, (b) spanwise, and (c) vertical velocities for the surface wave of $\lambda = 20$ cm at simulated time $t = 10T_0$. The contour levels are the same for the three velocities and equally distributed between $\pm 0.2\%$ of the linear phase velocity c_0 .

in which $\hat{\mathbf{v}}(x, l, \zeta, t)$ is the transverse Fourier component of \mathbf{v}' , l is the transverse wavenumber, and $\langle \cdot \rangle_x$ is a streamwise average. Since the length-scale variables are nondimensionalized by the reciprocal wavenumber of the surface wave k^{-1} , the nondimensional transverse wavenumber is $l_s = \lambda/d_s$ and is equivalent to the number of coherent vortex pairs (and also streaks) per wavelength λ .

The transverse characteristic length scale of coherent structures may also be deduced from an ensemble-averaged coherent structure. To proceed, the primitive positions of surface streaks are first located by searching the local maxima of temperature along cross-wave transects. A conditional average of a velocity component q is then defined as

$$\{q\}_c(\psi, \zeta, t) = \frac{1}{N_s} \sum_{i=1}^{N_s} q(x_i^s, y - y_i^s, \zeta, t), \quad (3)$$

where $(x_i^s, y_i^s, 0)$ is the coordinate of detected surface streak, and N_s is the total number of streaks detected. The streamwise vertical plane (x, y_i^s, ζ) therefore is considered to approximate the symmetric plane of a counterrotating vortex pair. The average, denoted by $\{\cdot\}_c$, is taken by shifting the cross-wave coordinate origin $\psi = 0$ to the position of a streak $y = y_i^s$.

Representative, conditional-averaged distributions of the three fluctuating velocity components for $\lambda = 20$ cm surface waves at $t = 10T_0$ are shown in Fig. 4. The result reveals an orderly cellular structure that is consistent with the qualitative properties of ideal Langmuir cells (Leibovich 1983). Some distinct features are, first, that the conditionally averaged streamwise velocity component is a maximum not at the surface but beneath it. This is sometimes referred to as a submerged jet (Fig. 4a). Second, the surface converging velocities are comparable to the downwelling velocities and larger than the submerged diverging velocities (Figs. 4b,c). Third, the downwelling velocities are larger than the upwelling velocities, and both decay rapidly with depth (Fig. 4c). Fourth, the maximum downwelling velocities are comparable to the surface velocity anomaly near the streak (Figs. 4a,c). Streak spacing d_s is determined by the width of a counterrotating vortex pair, that is, two cells, and so can be measured from the left and right extents where the spanwise velocity at the water surface vanishes.

Figure 5 depicts the temporal evolution of the non-dimensional transverse wavenumber for the predominant flow structure $l_s = \lambda/d_s$, that is, the number of coherent vortex pairs per wavelength for various wavelengths. This was estimated from the spectral power density distribution of the fluctuating velocities and from conditionally averaged distributions of spanwise velocity.

Both methods depict the same trend. Specifically that l_s decreases rapidly in the first few wave periods ($< 10T_0$) due to adjustment from the posed random noise to realistic fluid motions and then (over the next $20T_0$) stabilizes to a mean value about which it evolves. Accordingly, and consistent with that revealed by the isosurface distribution of streamwise vorticity in Fig. 3, l_s increases as the surface wave wavelength λ increases.

Measures of the characteristic transverse wavenumber given by the two methods, however, are not the same. Specifically, the transverse wavenumbers deduced from conditional-averaged velocity distribution are circa 20% smaller than those evaluated using the

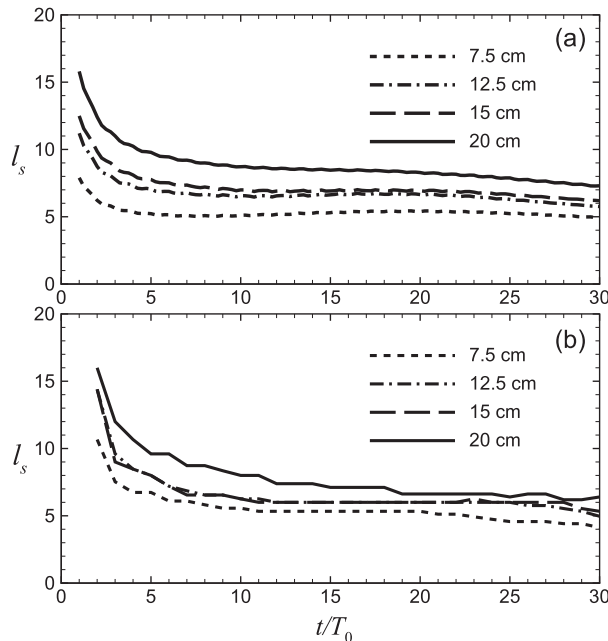


FIG. 5. Temporal evolution of the ratio of wavelength to dominant streak spacing for various wavelengths (indicated by different line types) estimated from (a) spectral density distribution of disturbance velocity and (b) cross-stream distribution of conditional-averaged spanwise velocity.

spectral power density of the velocity. This is because the process of conditional averaging acts to filter out the short wavelength finer structures. This feature is most evident for longer $\lambda = 20$ cm waves, as revealed in Fig. 3.

Looking now at Fig. 5a, we see that the characteristic transverse wavenumber for coherent disturbances per wavelength grows with increasing wavelength. Specifically, we see that l_s is about 5 to 6 for shorter progressive waves ($\lambda = 7.5$ cm), is approximately 7 for $\lambda = 12.5$ and 15 cm waves, and evolves from 9 at $t \approx 10T_0$ to around 8 at $t \approx 25T_0$ for $\lambda = 20$ cm. In fact, l_s would appear to scale as $\lambda^{1/2}$.

4. Wave-induced Eulerian mean flow

The results presented so far clearly reveal the formation of vortices or Langmuir cells beneath the free-propagating surface waves. Their presence begs the question whether they form via one of the instability mechanisms suggested by Craik and Leibovich (1976), in particular by the CL2 mechanism, which assumes a spanwise independent Lagrangian drift field in the presence of a sheared current of the same sign. Here, of course, our monochromatic waves generate an appropriate drift field, but, by design, there is no imposed Eulerian current, although, as we indicate below, the viscous action of the waves generates one.

First, according to potential theory for a free-propagating periodic wave of amplitude a and wave-number k , there is no mean Eulerian current up to second-order $O(\varepsilon^2)$, where $\varepsilon = ak$, but there exists a second-order mean Lagrangian drift:

$$u_s(z) = \omega_0 a^2 k e^{2kz} \equiv U_s e^{2kz} \quad (\varepsilon \ll 1). \quad (4)$$

This was first derived by Stokes (1847) and bears his name: the Stokes drift.

Second, a century later, Longuet-Higgins (1953) recognized that the viscous action of the waves give rise to a thin oscillatory boundary layer immediately next to the free surface that induces a mean stress. In turn, the stress gives rise to a second-order, Eulerian-mean flow \bar{u}_e oriented in the direction of wave propagation. Since details of the wave and oscillatory boundary layer vanish during the average, the stress must act within an $O(\varepsilon^2)$ range beneath the mean free surface, which, to leading order, is at the mean free surface $z = 0$, with

$$\frac{d\bar{u}_e}{dz} = 2\omega_0 \varepsilon^2 \quad (\varepsilon \ll 1). \quad (5)$$

The analysis was confirmed in experimental observations by Longuet-Higgins (1960) himself. Specifically, by using a filament of dye to visualize the near-surface mass transport, he observed a vertical gradient close to the summation attributed to both Lagrangian and Eulerian transport.

Figure 6 depicts the vertical distribution of averaged streamwise velocity $\langle u \rangle$ from the present numerical simulations and the corresponding profile of Stokes drift u_s [(4)], along with their vertical derivatives $d\langle u \rangle/dz$ and du_s/dz for surface waves of wavelength $\lambda = 7.5$ and 20 cm at three representative time instances.

In accord with the Stokes drift, the Eulerian-mean current likewise decays with depth (Fig. 6a) but is weaker than the drift near the surface ($\zeta > 0.8$). This weakness becomes more pronounced as the wavelength increases (Fig. 6b).

Turning now to the vertical differential of the Stokes drift and Eulerian flow (Figs. 6c,d), we see that except in close proximity to the surface, they also reveal similar trends. In contrast to the drift, however, which is a maximum at the free surface, the sheared Eulerian-mean current reaches its maximum several boundary layer thickness scales beneath the surface and then decreases with depth. Here, the boundary layer thickness scale is defined as $\delta = (2\nu/\omega_0)^{1/2}$ and is marked in Fig. 6d by dashes. The sheared Eulerian-mean current therefore has a maximum near the edge of the boundary layer and its value is close to the theoretical prediction of Longuet-Higgins (1953, 1960). This portion of the flow is shown in Figs. 6e and 6f.

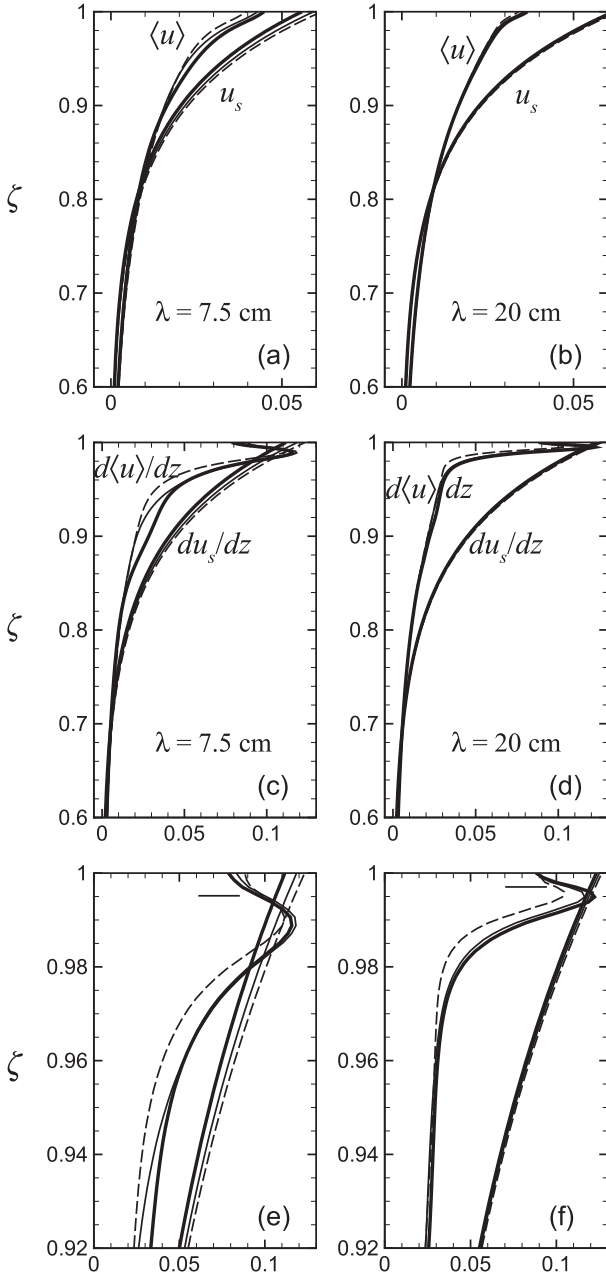


FIG. 6. Vertical distributions of (a),(b) averaged streamwise and Stokes drift velocities $\langle u \rangle$ and u_s and (c),(d) their vertical derivatives $d\langle u \rangle/dz$ and du_s/dz for the cases of $\lambda =$ (left) 7.5 and (right) 20 cm at three representative time instances $t = 5T_0$ (thin dashed line), $10T_0$ (thin solid line), and $30T_0$ (thick solid line). (e),(f) The zooms of (c) and (d) near the free surface. The corresponding thickness scales of the boundary layer, $\delta = (2\nu/\sigma)^{1/2}$, are marked by dashes in (e) and (f).

Finally, we note that because the differential drift and shear are of the same sign over much of the mixed layer, they satisfy the necessary (but not sufficient) condition shown by Phillips and Dai (2014) to excite the CL2 instability. Our task now is to determine whether the least

stable spanwise spacings given by instability theory are consistent with our spacings found numerically.

5. Stability analysis of CL equation

Craik (1982) noted that the shear [(5)] identified by Longuet-Higgins (1953) at the edge of the mean free surface is equivalent to a wave stress acting on the surface, which in turn generates a temporal, Eulerian-mean flow or current. Moreover, since such a current beneath free-propagating waves is, in appropriate circumstances, unstable to spanwise disturbances via the CL2 instability mechanism, Leibovich and Paolucci (1981) used the construct to explore the generation of Langmuir circulation. Our intent now is to revisit their construct and compare the results with those from our numerical simulations.

To proceed Leibovich and Paolucci (1981) employ the Craik and Leibovich (1976) or CL equations, which may be written as

$$\frac{\partial \mathbf{v}'}{\partial t} + w' \frac{\partial \bar{u}}{\partial z} \mathbf{i} = u_s \nabla_p u' - \nabla_p p' + \text{La} \nabla_p^2 \mathbf{v}', \quad (6)$$

where $\mathbf{v}'(y, z) = u' \mathbf{i} + v' \mathbf{j} + w' \mathbf{k}$ is the perturbed rotational velocity, p' is the perturbed pressure, and $\nabla_p = \partial/\partial y \mathbf{j} + \partial/\partial z \mathbf{k}$. These equations may be non-dimensionalized in various ways (Phillips and Dai 2014), but we employ a form in which the characteristic length scale $\mathcal{L} = k^{-1}$; the streamwise velocity is non-dimensionalized by the characteristic velocity scale $\mathcal{U} = u_*^2 \nu_T^{-1} k^{-1}$, where ν_T is the eddy viscosity; the spanwise and vertical velocities are nondimensionalized by $\mathcal{V} = U_s^{1/2} \mathcal{U}^{1/2}$; and the pressure is nondimensionalized by $\rho \mathcal{V}^2$. This form then exposes the Langmuir number defined as $\text{La} = \nu_T \mathcal{L}^{-1} \mathcal{V}^{-1}$.

The maximal eddy viscosity evaluated by $\nu_T = -\overline{u'w'}(d\bar{u}/dz)^{-1}$ at the early stage of the numerical simulation ($t \approx 5T_0$) is about $2 \times 10^{-3} \text{ cm}^2 \text{ s}^{-1}$, which is an order of magnitude less than the molecular viscosity ν . In consequence, the eddy viscosity ν_T in the Langmuir number may be replaced by molecular viscosity ν . The friction velocity associated with the wave stress [(5)] then becomes $u_* = (2\nu\omega_0)^{1/2} ak$, and the corresponding Langmuir number

$$\text{La} = \frac{\nu}{2^{1/2} a^2 \omega_0} = \frac{2\pi^{3/2} \nu}{g^{1/2} (ak)^2 \lambda^{3/2}}, \quad (7)$$

which is the reciprocal of wave Reynolds number.

Transverse instability of the rectified flow is then sought by assuming the disturbance to be spanwise periodic with wavenumber l and represented by the normal mode

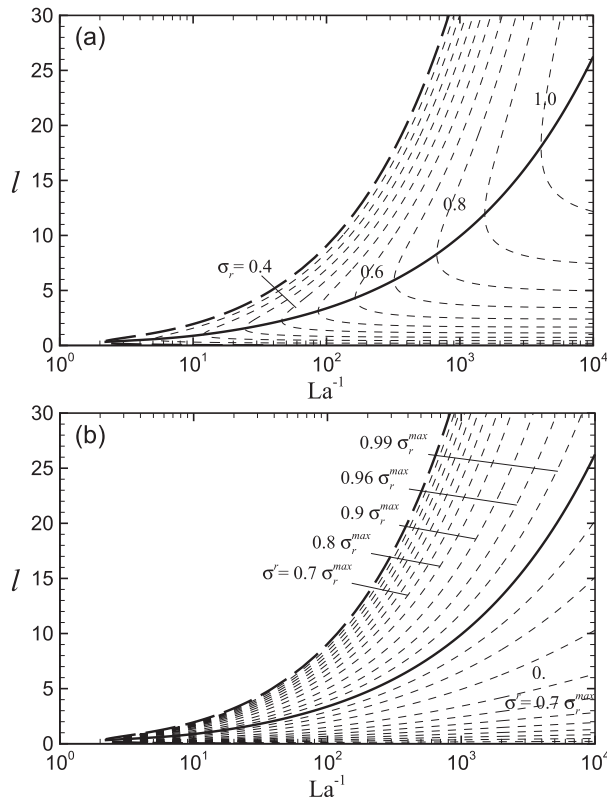


FIG. 7. Instability diagrams of the CL equation showing the range of unstable wavenumber l for varying reciprocal Langmuir number La^{-1} . The thick, long-dashed lines mark the margin of neutral stability $\text{Re}\{\sigma\} = 0$. Variation of the most unstable wavenumber with La^{-1} is depicted by a thick solid line. (a) Contour lines (thin, short-dashed lines) of various growth rates are superimposed on the unstable region; the nondimensional contours range from 0.1 to 10, and some are labeled on the corresponding contours. (b) Variations of unstable wavenumber with fractions of maximum growth rate (thin, short-dashed lines) are depicted. The fraction percentages are indicated on the corresponding lines.

$$[\mathbf{v}'(y, z), p'(y, z)] = [\hat{\mathbf{v}}'(z), \hat{p}'(z)] \text{Re}\{\exp(\sigma t + i l y)\}. \quad (8)$$

Here, the spanwise wavenumber l is equivalent to the ratio of the wavelength of surface wave wavelength λ to the wavelength of spanwise disturbance λ_d , that is $l = \lambda/\lambda_d$. Moreover the growth rate σ is complex and the transverse disturbance is unstable when $\text{Re}\{\sigma\} \equiv \sigma_r > 0$. Substituting (8) into the linearized CL equation (6) results in a system of ordinary differential equations that are solved for σ , $\hat{\mathbf{v}}'(z)$, and $\hat{p}'(z)$, given the spanwise wavenumber l and the Langmuir number La . The equations are solved in the manner of Leibovich and Paolucci (1981) using Galerkin techniques, albeit with refinements introduced by Phillips (2001a), such as orthogonal shape functions (Chebyshev polynomials). The numerical procedure is then carried out by solving a generalized complex

eigensystem for the truncated polynomial coefficients as the eigenvector and σ as the eigenvalue.

6. Stability results

Stability diagrams for the wavenumber l and a range of reciprocal Langmuir number La^{-1} are presented in Fig. 7 for a mean velocity profile driven by a surface stress with a vertical shear given by (5). The thick, long-dashed lines mark the margin of neutral stability $\sigma_r = 0$. Variation of the most unstable wavenumber l_{max} with La^{-1} is depicted by the thick, solid line. Contour lines of various growth rates are superimposed on the instability region in Fig. 7a, and variations of unstable wavenumber with various fractions of the maximum growth rate are depicted in Fig. 7b. The flow is globally stable for $La^{-1} \lesssim 2.14$. Note that this is higher than the 1.46 and 1.4395 globally stable values reported, respectively, by Leibovich and Paolucci (1981) and Phillips (2001a) because of a factor of 2 difference in the magnitude of the Stokes drift. Above this critical reciprocal Langmuir number, the range of the unstable wavenumber increases monotonically.

Further insight into the growth rates is obtained by presenting the results in the three-dimensional form $\sigma_r = \sigma_r(La^{-1}, l)$, as shown in Fig. 8. It reveals that the most unstable wavenumber l_{max} , as well as its growth rate σ_r^{max} , increases with La^{-1} but that the increasing rates decrease asymptotically. More importantly, we see that the growth rate varies insignificantly for a large range of wavenumbers near the most unstable modes. For example, although the wavenumber of the least stable mode at $La^{-1} = 5000$ is $l_{\text{max}} \approx 20$, wavenumbers with growth rates greater than 90% of the maximum extend from $l \approx 8$ to 36.

Now if the longitudinal vortical structures observed in our numerical simulations and those in the experiment of Savel'ev et al. (2012) are induced by the CL2 instability mechanism, then the dominant spacing for a pair of coherent vortices should be close to the spacing specified by the least stable wavenumber, that is, $l_s \approx l_{\text{max}}$, and is, as we see in Fig. 9.

Looking first to our numerical results, we see for the shortest progressive wavelength simulated ($\lambda = 7.5$ cm) that l_s almost coincides with l_{max} . The two deviate for the other longer waves simulated ($\lambda = 12.5, 15,$ and 20 cm), but not significantly, and in all cases remain within a range in which the growth rate is 96% to 97% of the maximum.

Accordingly, the wavenumbers of the predominant streak spacings estimated from the autocorrelation function of surface streamwise or spanwise velocities in the experiments of Savel'ev et al. (2012) are also in close

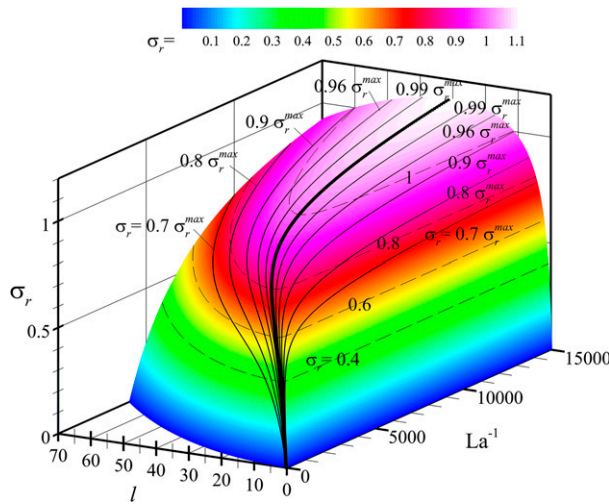


FIG. 8. Three-dimensional instability diagrams of the CL equation showing the distribution of growth rate σ_r for the unstable range of unstable wavenumber l and reciprocal Langmuir number La^{-1} . The filled contour depicts the distribution of growth rate; some labeled contour lines (thin dashed lines) are superimposed. Variations of unstable wavenumber with fractions of maximum growth rate (thin solid lines) are also superimposed. The fractions are indicated on the corresponding contour lines.

proximity to the wavenumbers of the least stable disturbances predicted from linear stability theory. Here, there is more scatter, but the l_s are largely within the range of the unstable wavenumbers with at least 90% of the maximum growth rate.

Finally, we note that results from both the numerical simulations and experiment are all smaller than the transverse wavelengths of the most unstable disturbances $l_s < l_{max}$; that is, the computed and measured spacings between coherent vortex pairs are wider than the predicted wavelengths. This does not preclude the presence of more closely spaced vortices but rather suggests our method for isolating the spacing is optimized to isolate the largest spacing and effectively filters out finer structures in the process.

7. Discussion

Analysis of the numerically simulated flow field beneath progressive, irrotational, monochromatic, free-propagating surface waves reveals the presence of arrays of counterrotating coherent vortex pairs much like Langmuir circulation beneath wind-driven surface waves (Tsai et al. 2015). The surface footprints of these vortices appear as elongated streaks, which are also observed experimentally (Savelyev et al. 2012). Although no mean shear flow is imposed in the simulations, they generate, in accord with the analysis of

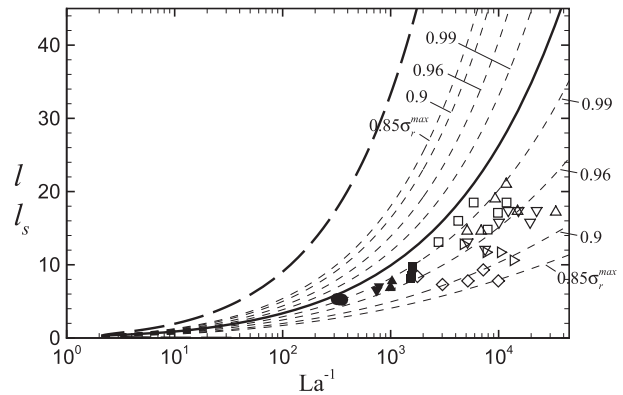


FIG. 9. Comparison of the unstable wavenumbers predicted from linear stability analysis of CL equation (solid and dashed lines as described in Fig. 7b) with the nondimensional dominant streak spacing computed from the present numerical simulations (solid symbols; \blacksquare : $\lambda = 20$ cm, \blacktriangle : $\lambda = 15$ cm, \blacktriangledown : $\lambda = 12.5$ cm, and \bullet : $\lambda = 7.5$ cm) and from experimental measurements by Savelyev et al. (2012) (open symbols; \square : $\lambda = 140$ cm, \triangle : $\lambda = 119$ cm, ∇ : $\lambda = 99$ cm, \triangleright : $\lambda = 81$ cm, and \diamond : $\lambda = 64$ cm). Simulated results at three representative time instances, $t = 5T_0, 15T_0, 25T_0$, are shown; the corresponding reciprocal Langmuir number La^{-1} varies from small to large though the variation is very small.

Longuet-Higgins (1953), an Eulerian-mean shear flow of magnitude comparable with that of the Stokes drift, induced by the waves.

Since Craik and Leibovich (1976) theory indicates that mean shear and drift are key to the formation of Langmuir circulation and since both shear and drift are present in our simulation, we then question whether our findings concur with instability theory based upon the CL equation. Of particular interest is the CL2 instability, which requires spanwise-independent drift, as arises in our imposed monochromatic waves. Instability is tripped by a cross-stream anomaly in mean shear.

We question first whether the dominant spacings between coherent vortex pairs deduced from the numerical simulation and laboratory experiments concur with spacings predicted by linear stability analysis and begin with the simulations (Fig. 9, solid symbols). We find that there is a preferred lateral spacing and see that agreement with the least stable (solid line) is remarkably good. But that is not the complete story because stability analysis further indicates that energy will focus not at one specific transverse wavenumber but rather any one of a broad spectrum of wavenumbers of comparable growth rate. These are shown as dashed lines. This occurrence blurs the notion of preferred spacing because once instability locks onto a specific wavenumber in this spectrum, it will stay there.

In an experiment, therefore, where cross-stream anomalies in mean shear can arise for a variety of reasons, we would expect instability to be triggered over a broad range of spacings. Of course, the vortices that survive will be those of the highest growth rate, and that is what we see in Fig. 9 (open symbols), where the growth rates for all spacings measured by Savelyev et al. (2012) are at least 85% of that of the least stable mode.

So are the vortices observed in our simulation excited by the CL2 instability? It is very likely. CL2 is an (initially) exponentially growing wave-driven inviscid centrifugal instability (Phillips 1998). If we question each requirement, we note, first, that the initial growth of the vortices is indeed exponential, and, second, that because the mean shear is wave driven, the vortices too are wave driven. To determine the role of viscosity, however, we would need to repeat the calculations at much lower La^{-1} , which we have not done. Nevertheless, the transverse wavenumbers excited in the simulation are consistent with unstable modes predicted by linear instability theory, and we conclude that the underlying instability therein is the CL2 instability. Together, these features provide the first evidence that the CL2 instability is realizable. With that in mind, and knowing that the transverse wavenumbers excited in the experiments of Savelyev et al. (2012) are likewise consistent with linear instability theory, we infer that their experiments provide the first experimental evidence that the CL2 instability is realizable.

Finally, we note that although energy will initially focus at any one of a spectrum of transverse wavenumbers in accord with linear stability theory, nonlinearities will at some stage spawn smaller-scale structures. Since they too can experience growth rates comparable with that of the initial structure, the process highlights an efficient direct cascade of energy into smaller scales. This feature has broad implications with regard to transition from laminar to turbulent flow (Ardhuin and Jenkins 2006; Babanin 2006) and is evident in our numerical simulations, albeit not at the free surface.

Acknowledgments. We acknowledge Dr. Shi-ming Chen for conducting the computations of conditional average described in section 3. This work was supported by grants from Taiwan Ministry of Science and Technology under Contracts MOST 104-2611-M-002-005-MY3 and 105-2923-M-002-006-MY3.

REFERENCES

- Ardhuin, F., and A. D. Jenkins, 2006: On the interaction of surface waves and upper ocean turbulence. *J. Phys. Oceanogr.*, **36**, 551–557, doi:10.1175/JPO2862.1.
- Babanin, A. V., 2006: On a wave-induced turbulence and a wave-mixed upper ocean layer. *Geophys. Res. Lett.*, **33**, L20605, doi:10.1029/2006GL027308.
- Craik, A. D. D., 1982: The drift velocity of water waves. *J. Fluid Mech.*, **116**, 187–205, doi:10.1017/S0022112082000421.
- , and S. Leibovich, 1976: A rational model for Langmuir circulations. *J. Fluid Mech.*, **73**, 401–426, doi:10.1017/S0022112076001420.
- Langmuir, I., 1938: Surface motion of water induced by wind. *Science*, **87**, 119–123, doi:10.1126/science.87.2250.119.
- Leibovich, S., 1983: The form and dynamics of Langmuir circulations. *Annu. Rev. Fluid Mech.*, **15**, 391–427, doi:10.1146/annurev.fl.15.010183.002135.
- , and S. Paolucci, 1981: The instability of the ocean to Langmuir circulation. *J. Fluid Mech.*, **102**, 141–167, doi:10.1017/S0022112081002589.
- Longuet-Higgins, M. S., 1953: Mass transport in water waves. *Philos. Trans. Roy. Soc. London*, **A245**, 535–581, doi:10.1098/rsta.1953.0006.
- , 1960: Mass transport in the boundary at a free oscillating surface. *J. Fluid Mech.*, **8**, 293–306, doi:10.1017/S002211206000061X.
- Melville, W. K., R. Shear, and F. Veron, 1998: Laboratory measurements of the generation and evolution of Langmuir circulations. *J. Fluid Mech.*, **364**, 31–58, doi:10.1017/S0022112098001098.
- Phillips, W. R. C., 1998: Finite-amplitude rotational waves in viscous shear flows. *Stud. Appl. Math.*, **101**, 23–47, doi:10.1111/1467-9590.00084.
- , 2001a: On the instability to Langmuir circulations and the role of Prandtl number and Richardson numbers. *J. Fluid Mech.*, **442**, 335–358, doi:10.1017/S0022112001005110.
- , 2001b: On the pseudomomentum and generalized Stokes drift in a spectrum of rotational waves. *J. Fluid Mech.*, **430**, 209–220, doi:10.1017/S0022112000002858.
- , 2002: Langmuir circulations beneath growing or decaying surface waves. *J. Fluid Mech.*, **469**, 317–342, doi:10.1017/S0022112002001908.
- , 2005: On the spacing of Langmuir circulation in strong shear. *J. Fluid Mech.*, **525**, 215–236, doi:10.1017/S0022112004002654.
- , and Z. Wu, 1994: On the instability of wave-catalysed longitudinal vortices in strong shear. *J. Fluid Mech.*, **272**, 235–254, doi:10.1017/S0022112094004453.
- , and Q. Shen, 1996: A family of wave-mean shear interactions and their instability to longitudinal vortex form. *Stud. Appl. Math.*, **96**, 143–161, doi:10.1002/sapm1996962143.
- , and A. Dai, 2014: On Langmuir circulation in shallow waters. *J. Fluid Mech.*, **743**, 141–169, doi:10.1017/jfm.2014.37.
- Plueddemann, A. J., J. A. Smith, D. M. Farmer, R. A. Weller, W. R. Crawford, R. Pinkel, S. Vagle, and A. Gnanadesikan, 1996: Structure and variability of Langmuir circulation during the surface waves processes program. *J. Geophys. Res.*, **101**, 3525–3543, doi:10.1029/95JC03282.
- Savelyev, I. B., E. Maxeiner, and D. Chalikov, 2012: Turbulence production by nonbreaking waves: Laboratory and numerical simulations. *J. Geophys. Res.*, **117**, C00J13, doi:10.1029/2012JC007928.
- Stokes, G. G., 1847: On the theory of oscillatory waves. *Trans. Cambridge Philos. Soc.*, **8**, 441–455.
- Teixeira, M., and S. Belcher, 2002: On the distortion of turbulence by a progressive surface wave. *J. Fluid Mech.*, **458**, 229–267, doi:10.1017/S0022112002007838.
- Tsai, W.-T., and L.-P. Hung, 2007: Three-dimensional modeling of small-scale processes in the upper boundary layer bounded

- by a dynamic ocean surface. *J. Geophys. Res.*, **112**, C02019, doi:[10.1029/2006JC003686](https://doi.org/10.1029/2006JC003686).
- , S.-M. Chen, and C.-H. Moeng, 2005: A numerical study on the evolution and structure of a stress-driven, free-surface turbulent shear flow. *J. Fluid Mech.*, **545**, 163–192, doi:[10.1017/S0022112005007044](https://doi.org/10.1017/S0022112005007044).
- , —, G.-H. Lu, and C. S. Garbe, 2013: Characteristics of interfacial signatures on a wind-driven gravity-capillary wave. *J. Geophys. Res. Oceans*, **118**, 1715–1735, doi:[10.1002/jgrc.20145](https://doi.org/10.1002/jgrc.20145).
- , —, and —, 2015: Numerical evidence of turbulence generated by nonbreaking surface waves. *J. Phys. Oceanogr.*, **45**, 174–180, doi:[10.1175/JPO-D-14-0121.1](https://doi.org/10.1175/JPO-D-14-0121.1).
- Veron, F., and W. K. Melville, 2001: Experiments on the stability and transition of wind-driven water surfaces. *J. Fluid Mech.*, **446**, 25–65.